Integrated Wireless Charging Receiver for Electric Vehicles With Dual Inverter Drives

Sepehr Semsar, *Member, IEEE*, Zhichao Luo, *Member, IEEE*, Shuang Nie, *Member, IEEE*, and Peter W. Lehn, *Senior Member, IEEE*

***Abstract*—Wireless/contactless charging of electric vehicles can improve the safety and convenience of the electric vehicle charging process. However, in order to enable wireless charging on an electric vehicle, additional components need to be added to the vehicle, which increase the cost, and weight of the vehicle. Specifically, a wireless receiver coil and power electronics are required to receive the wireless power and charge the battery. This work proposes a new integrated wireless charger, which reuses the existing drivetrain components, such as the traction inverters and the motor, to serve as the receiver-side power electronics for wireless charging. Importantly, this topology limits the high frequency currents entering the traction components, such as the motor, which are susceptible to high frequency losses. The drivetrain can serve to control the charging rate of the batteries, which eliminates the need for transmitter side battery charging control and communication. Experimental validation was done by coupling a 110 kW EV machine and dual-inverter drivetrain to a 6.6 kW wireless transmission system. A peak charging efficiency of 94.3% over a vertical coil distance of 200 mm was achieved.**

***Index Terms*—Battery charging, dual-inverter, electric vehicle, integrated charging, motor drives, wireless charging.**

I. Introduction

INTEGRATED on-board charging has recently gained significant interest in both academia and industry, due to the potential cost and weight savings in the vehicle [1], [2], [3], [4], [5], [6], [7]. Integrated charging involves repurposing the existing drivetrain components, namely, the power electronics and motor, to serve as part of the charging system. In doing so, this can eliminate additional power electronics and magnetics (and their associated cooling requirements, connectors, and enclosures) required for charging from an ac grid. Another common advantage of integrated chargers are their high charging power. As integrated chargers use the high power traction power electronics and motor, they can be capable of processing over 100 kW of power. Therefore, when used for charging, they can allow higher charging currents, resulting in faster charging speeds.

Manuscript received 9 March 2023; revised 1 July 2023; accepted 12 September 2023. Date of publication 29 September 2023; date of current version 6 December 2023. This work was supported by the Natural Sciences and Engineering Research Council of Canada (NSERC), under Grant CRDPJ 513206-17. Recommended for publication by Associate Editor A. P. Hu. *(Corresponding authors: Sepehr Semsar; Zhichao Luo.)*

Sepehr Semsar, Shuang Nie, and Peter W. Lehn are with the Department of Electrical and Computer Engineering, University of Toronto, Toronto, ON M5S3G4, Canada (e-mail: sep.semsar@mail.utoronto.ca; shuang.nie@mail.utoronto.ca; lehn@ece.utoronto.ca).

Zhichao Luo is with the School of Electric Power Engineering, South China University of Technology, Guangzhou 510640, China, and also with the Department of Electrical and Computer Engineering, University of Toronto, Toronto, ON M5S3G4, Canada (e-mail: hgzcluo@scut.edu.cn).

Color versions of one or more figures in this article are available at https://doi.org/10.1109/TPEL.2023.3320664.

Digital Object Identifier 10.1109/TPEL.2023.3320664

Various integrated chargers have been proposed in literature, based on different drivetrain configurations. A simple solution proposed in [8] demonstrated ac charging from a single phase grid by connecting the grid through a diode bridge between the motor's neutral point and the negative dc terminal of the battery. In this case, the traction inverter was operated as a three-phase power factor correction (PFC) boost converter. Renault's commercially sold integrated charging solution involves using a current source converter front-end to interface the drivetrain to the grid [9], [10]. An interesting topology based on the dual-inverter drive architecture was introduced in [11], where a silicon carbide (SiC) active front end was added to allow bidirectional ac charging at up to 19.2 kW. Peak efficiencies of 97% were reported.

While conductive charging is the most common charging method used today in most EVs, inductive wireless charging has also been gaining popularity for its improved convenience and safety [12]. While theoretically not as efficient as conductive charging, some applications benefit greatly from wireless charging, such as transit vehicles, autonomous vehicles, as well as vehicles operating in harsh conditions [13]. A significant amount of research exists on improving the transmission efficiency of wireless chargers, especially under misaligned conditions [14], [15], [16], [17], [18], [19]. In [17], the losses associated with transmitter-receiver coil misalignment were reduced by employing field-oriented control to direct the magnetic field toward the receiver. However, wireless charging systems are usually very expensive and low power compared with even single-phase ac charging. This has hindered the industrial adoption of wireless charging solutions, and needs to be addressed. In some instances, cost and weight savings on-board the car are made by placing a passive, rectifying converter on-board the car, and having the off-board transmitter power electronics perform the necessary charge control. This means the controller feedback variables must be transmitted from the vehicle to the transmitter, using a form of wireless communication in real time. This can pose a challenge for the robustness and security of the vehicle/charger [20].

In order to eliminate the need for wireless communication of sensitive controller feedback signals, the authors in [21], [22], [23], [24], [25], and [26] have implemented the control

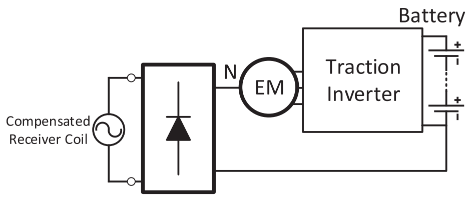

Fig. 1. Integrated wireless charger proposed in [29], which utilizes the drivetrain.

on the receiver (on-board) side. However, in all of these cases, the converters on-board the vehicle become significantly more complex and expensive, making it prohibitive to scale up the charging power.

Integrated wireless charging systems can reduce the cost associated with on-board discrete wireless charging power electronics, while enabling higher charging power. Integration of wireless charging is only recently being investigated. In [27], the inductor required for the receiver side power electronics was integrated with the receiver coil, reusing the ferrite cores of the coils. However it still requires additional litz wire, which is expensive. The work in [28] took this a step further by repurposing the vehicles on-board single-phase charger to perform the majority of the receiver side charge control. This can be a large cost savings, however it still requires a traditional on-board single phase ac charger and is limited to the power of that charger (usually around 6.6 kW). In [29], better integration was achieved by connecting the wireless receiver coil through a diode bridge between the neutral point of the motor and the negative dc terminal of the battery, as shown in Fig. 1. This seems to build on the integrated single phase charger in [8]. However, this necessitates an additional diode bridge, and it still requires traditional transmitter side control. Furthermore, it requires that the drivetrain carry high frequency wireless charging currents, which will either substantially degrade efficiency, or require costly optimization of the drivetrain to limit high frequency losses. The solution presented in [30] directly uses the traction inverter to perform ac charging, driving, and wireless charging. It relies on contactors to connect either the motor, ac grid, or the wireless coil to the traction inverter. A disadvantage of this configuration is the requirement of several high current, multipole contactors, which are large and expensive. Furthermore, the traction inverter must be compatible with the high frequency currents of the wireless coil, meaning it must be designed with wide-band gap devices.

In this work, a new, completely integrated wireless charger, is proposed and shown in Fig. 2. Similar to the integrated charger proposed in [29] and [30], it builds upon a standard drivetrain topology. The proposed integrated charger in this work builds upon a dual inverter drive. The integrated charger consists of several important blocks; the dual inverter drive, which consists of two traction inverters, two batteries, and an open winding machine, as well as the proposed connection to the compensated wireless receiver coil. The proposed connection requires two small capacitors as well as four switches (in this case, diodes). This approach not only saves cost of the power electronic components themselves, but also on the secondary requirements, such

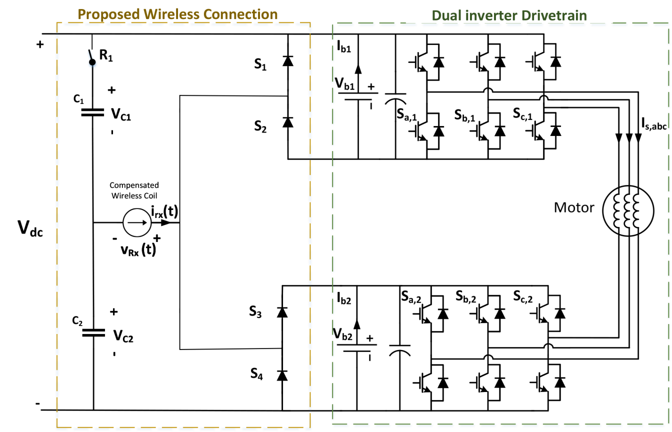

Fig. 2. Proposed integrated wireless charger, which re-uses the switches (S_1–S_4) introduced in [11] for wireless charging.

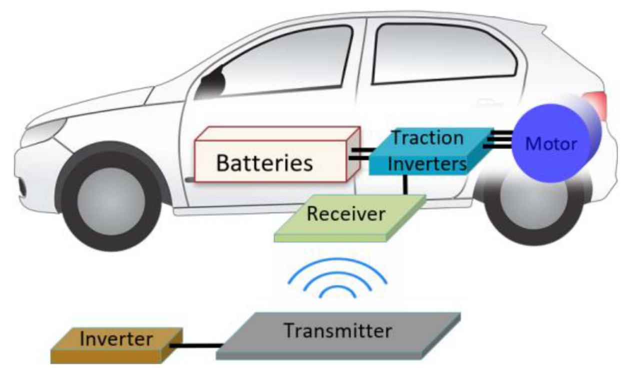

Fig. 3. Proposed integrated wireless charging system on an EV.

as liquid cooling plates, controller board, sensors, protection, battery contactors, enclosures, and connectors. It should be noted that in [11], it was shown that the four added switches can also be used to perform integrated single-phase ac charging, which can also eliminate the on-board charger; an improvement over the solution proposed in [28] that requires a discrete on-board charger. This also improves utilization of the added switches S_1, S_2, S_3, and S_4, further improving the value-add of the system. The proposed solution can also restrict the high frequency currents of the wireless charging system from entering the drivetrain, unlike the solution proposed in [29] and [30]. The proposed solution is shown in the context of an EV in Fig. 3.

A wireless charging specific advantage of this topology is that the power electronics on the drivetrain can be leveraged to operate like a voltage doubler. This halves the voltage on the receiver coil, which in turn means less flux is required from the transmitter coil. This will improve wireless transmission efficiency as it results in a lower current in the wireless transmitter coil, which is often physically large with many turns, and therefore subject to high ohmic losses [31].

II. Proposed Topology

A challenge with using an integrated charger as the power electronics for a wireless system is the high frequency requirements of the wireless power transfer. Nominally, the standard

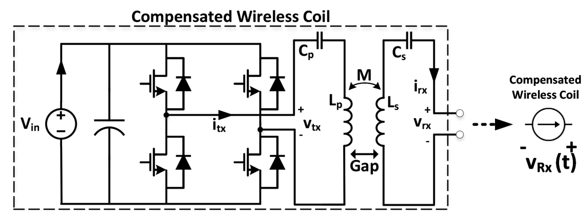

Fig. 4. Implementation of the wireless power transmission system.

for wireless power transfer recommends a frequency of 85 kHz. From the drivetrain's perspective, this high frequency current can create significant losses. The large IGBT-based traction inverters cannot switch that fast due to the large device tail currents, and the motor magnetics may incur significant core loss. The motor windings will also incur significant resistive losses, due to the skin effect phenomenon. As such, the drivetrain operating frequency must be kept low, and within the conventional operating range.

The proposed topology configuration meets a critical objective: the high frequency wireless currents do not enter the dual inverter drive, they rather remain confined within the diodes and the capacitors. SiC diodes can be used, which meet the current rating of the wireless charging coil, and they can be mounted on the same cooling heatsink as the traction inverters. Normally, a challenge associated with dual inverter drives is that two isolated batteries are used, making them incompatible with existing charging solutions. The proposed topology and control also addresses this challenge.

A. Wireless Coil Topology

The wireless power transmission system is shown in Fig. 4, and is the specific implementation of the compensated receiver coil modeled as a current source in Fig. 2. In this case, the coils are rectangular coils. The transmitter coil is excited using a full bridge converter that induces a voltage, over a gap of 200 mm, onto the receiver coil. Finally, the compensated receiver coil is connected to the integrated wireless charger. The detailed parameters are described later in Table II. The dc-bus voltage (V_{in}) is determined based on the coil parameters, and is a fixed value during operation. Due to the compensation strategy, the receiver acts as a current source, whose value is set by the dc-bus voltage (V_{in}) on the transmitter side. Hence, the receiver current is fixed and at a nominal value. More information regarding different compensation techniques can be found in [32].

B. Principle of Operation

The integrated charger will have four main modes of operation: Standby mode, passive mode, active mode A, and active mode B. The main difference between these operating modes are how the traction inverters are controlled. Therefore, before investigating each mode in detail, its important to describe the operating principle of the traction inverters.

The traction inverters, shown in Fig. 5 are operated as a multilevel, multiphase dc/dc converter. This can be shown by considering the set of usable switching states, given in Table I. It can be seen that based on the switches enabled, the output

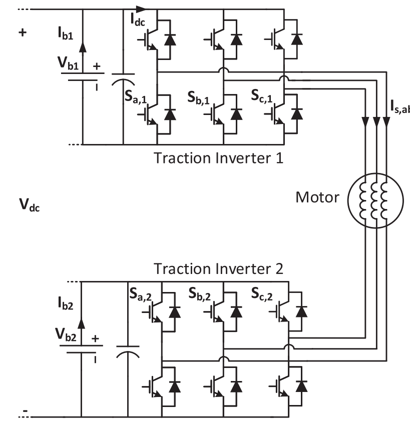

Fig. 5. DC–DC stage implemented using the traction inverters and motor.

TABLE I
DC–DC STAGE SWITCHING STATES

State	S_{a1}	S_{a2}	v_L	V_{dc}
a	0	0	V_{dc}	0
b	0	1	$V_{\text{dc}} - V_{b2}$	V_{b2}
c	1	0	$V_{\text{dc}} - V_{b1}$	V_{b1}
d	1	1	$V_{\text{dc}} - V_{b1} - V_{b2}$	$V_{b1} + V_{b2}$

voltage (V_{dc}) can be anywhere between zero and the sum of both batteries. Consequently a relationship can be derived for the output voltage (V_{dc})

$$V_{\text{dc}} = D(V_{b1} + V_{b2}) \tag{1}$$

where D is a common duty cycle sent to switches $S_{a,1}, S_{b,1}, S_{c,1}$ and $S_{a,2}, S_{b,2}, S_{c,2}$. Note that each half-bridge itself is operated in a complementary manner.

In this case, the motor windings serve as the main filtering element, defining the amplitude of ripple current in the dc/dc converter. This raises two potential concerns: 1) the motor might generate torque and 2) the motor inductance is usually small, therefore it might lead to high ripple.

Torque generation is avoided in a permanently excited machine by ensuring the phase currents are equal. Based on the Clarke transform, this equates to a zero sequence current, which does not produce torque. In a symmetrical machine, zero sequence current can be driven by applying the same duty-cycle to each phase.

With respect to the ripple current, there are two ripple currents of concern: the phase ripple current and the output ripple current. Due to its multiphase nature, the output current (I_{dc}) is defined as

$$I_{\text{dc}} = I_{sa} + I_{sb} + I_{sc}. \tag{2}$$

Due to the multilevel and multiphase nature of the dual inverter drive, two types of interleaving strategies can be applied to minimize the ripple current. The first interleaving strategy can be employed by phase shifting the carrier of the top and bottom gating signals (S_{a1} and S_{a2}) by 180°. Looking at the switching states in Table I, this enables states "b" and "c," which apply a smaller voltage step across the motor inductance. This can increases the effective ripple frequency across the motor inductance to be at twice the switching frequency of the traction inverters (f_{sw}). The next interleaving strategy leverages the multiphase nature of the traction inverters. As the output current is the sum of the individual phase currents, if the ripple of the phase currents are phase shifted by 120°, then the output ripple frequency will be at an effective of three times f_{sw}. The combination of both interleaving strategies can increase the effective ripple frequency seen at the output (I_{dc}) to be up to $6f_{\text{sw}}$. A more rigorous analysis of interleaving strategies are done in [33] for a similar dc–dc converter. Note the "V_{dc}" column in Table I is not the average value, rather the switched voltage across the smoothing capacitors C_1, C_2. Practically, the ripple frequency is important for reducing the size of capacitors C_1, C_2, which serve to smooth the voltage across the wireless receiver coil.

The ripple across the motor inductance can be derived by applying Kirchoffs voltage law. Neglecting parasitic resistances, and considering phase "a" as an example, the voltage across the inductor can be written as

$$v_L(t) = V_{\text{dc}} - V_{b1}(S_{a1}) - V_{b2}(S_{a2}). \tag{3}$$

Finally, the analytical equation for the inductor ripple can be written as

$$\Delta i_L(t) = \begin{cases} \frac{(V_{\text{dc}}-V_{b1})D}{f_{\text{sw}} L_s} & \text{if } 0 < \text{D} < 0.5 \\ \frac{(V_{\text{dc}}-V_{b1})(1-D)}{f_{\text{sw}} L_s} & \text{if } 0.5 < \text{D} < 1 \end{cases} \tag{4}$$

where L_s is the leakage inductance of the motor.

It is interesting to note that (4) implies that the inductor current ripple, $\Delta i_L(t)$, will change as V_{dc} is varied. As the ripple current impacts the dc/dc stage efficiency, it should be understood in order to perform optimization of the wireless charging system. For example, since the system has the least ripple (and highest efficiency) at $D = 0$, $D = 0.5$, and $D = 1$, the wireless charging system should be designed such that the dc/dc stage operates in those regions, for the majority of the charging period.

1) Standby Mode: Unlike most dc–dc converters, a useful operating mode in this case is when

$$S_{a,1} = S_{b,1} = S_{c,1} = 0$$
$$S_{a,2} = S_{b,2} = S_{c,2} = 0. \tag{5}$$

According to (1), this sets the voltage $V_{\text{dc}} = 0$ and thus sets the receiver coil voltage (v_{rx}) to zero. This effectively bypasses the receiver coil and stops the charging of the batteries. As the series-compensated wireless receiver coil behaves like a current source, attempting to stop charging by open-circuiting it will cause an over-voltage condition. Standby mode is useful since it simultaneously places the receiver coil in a safe state, while stopping the charging process of the batteries, regardless of the status of the off-board wireless charging transmitter.

2) Passive Mode: Passive mode can be enabled by not utilizing the traction inverters as a dc/dc stage (i.e., gating is disabled on the traction inverters) and is shown in Fig. 6. This mode of operation can be used when the charging controllers request the maximum possible charging power or when battery charge control is performed off-board the vehicle (e.g., via the wireless transmitter). This is an advantageous operating mode, as it eliminates all the losses associated with the switching of the traction inverters and the motor. In order to understand the operation of passive mode, the conduction paths can be traced when the receiver current is positive ($i_{\text{rx}} > 0$) and negative ($i_{\text{rx}} < 0$). These are shown in Fig. 6(a) and (b), respectively. It can be seen that during each half of the conduction cycle, two parallel paths exist, namely, Paths "A" and "B" and Paths "C" and "D."

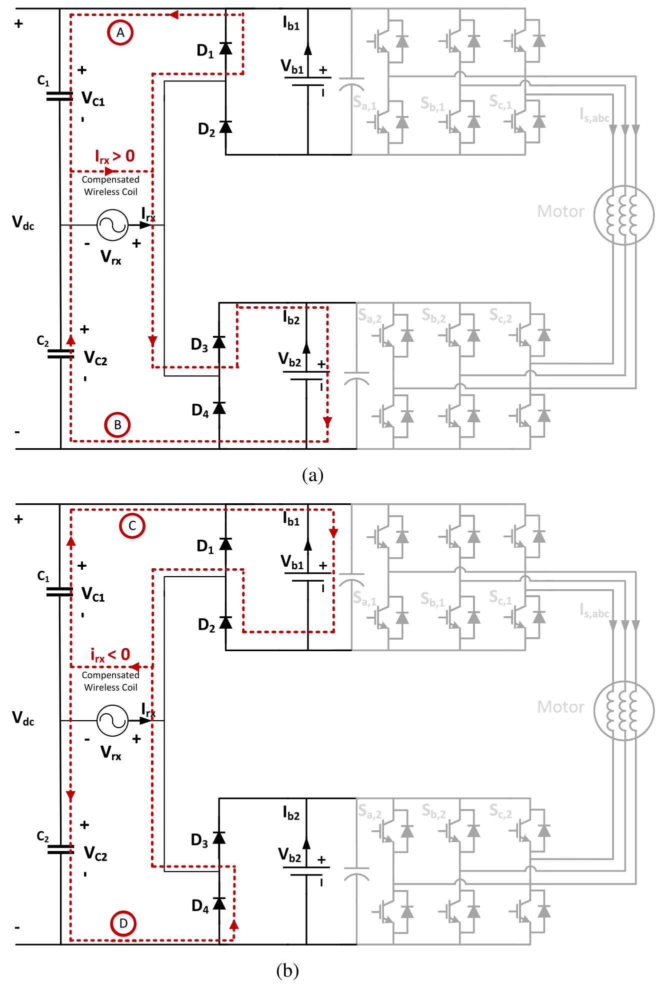

Fig. 6. Dual inverter integrated charging circuit during passive operating mode, where the traction inverters and the motor are not involved in the charging operation. (a) Conduction path during positive half cycle ($i_{\text{rx}} > 0$. (b) Conduction path during negative half cycle ($i_{\text{rx}} < 0$).

These paths are redrawn in a simplified manner in Fig. 7. Considering the case when $i_{\text{rx}} > 0$ [shown in Fig. 7(a)], it can be seen that the two parallel paths include a diode. The series diodes determine, which path the current will flow, and consequently, determine the back-emf voltage of the receiver coil, v_{rx}. Since there are two diodes in parallel, the path which requires the lowest voltage will be established and the receiver back-emf voltage will be clamped to that voltage, meaning the other path cannot exist simultaneously. The condition to forward bias each diode can be written as

$$\text{Path "A"}, D_1 \text{ ON} : V_{C1} < V_{b2} - V_{C2} \tag{6}$$

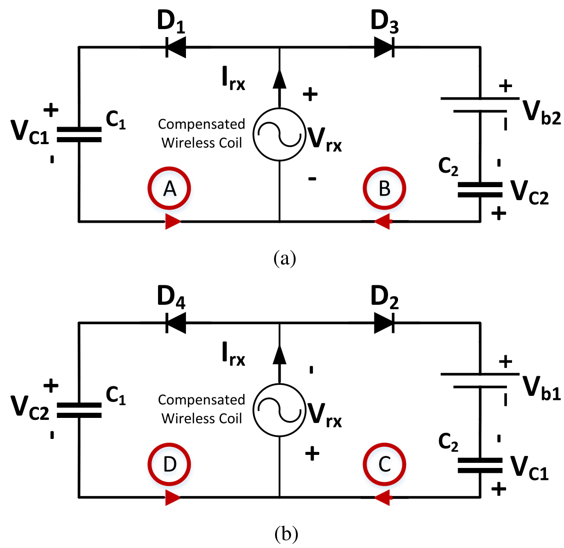

Fig. 7. Simplified circuit during passive operating mode. (a) Conduction path during positive half cycle ($i_{\rm rx} > 0$). (b) Conduction path during negative half cycle ($i_{\rm rx} < 0$).

$$\text{Path “B”}, D_3 \text{ ON} : V_{C1} > V_{b2} - V_{C2}. \tag{7}$$

Consequently, that can be used to determine the applied back-emf applied to the receiver coil when each path is active

$$v_{\rm rx} = \begin{cases} V_{C1} & \text{Path “A”} \\ V_{b2} - V_{C2} & \text{Path “B”}. \end{cases} \tag{8}$$

In (8) when the current is positive ($i_{\rm rx} > 0$), the back-emf voltage will be clamped by either the diodes in Path “A” or Path “B.” A generalized equation considering the clamping effect of the diodes can be written as

$$v_{\rm rx} = \text{Min}(V_{C1}, V_{b2} - V_{C2}) \text{ for } i_{\rm rx} > 0. \tag{9}$$

In this case, a minimum function is used to capture the clamping behavior of the diode path, which requires the least voltage to conduct. Similarly, when the current is negative ($i_{\rm rx} < 0$), the back-emf can be derived as

$$v_{rx} = \begin{cases} V_{C1} - V_{b1} & \text{Path “C”} \\ -V_{C2} & \text{Path “D”} \end{cases} \tag{10}$$

$$v_{rx} = -\text{Min}(V_{C2}, V_{b1} - V_{C1}) \text{ for } i_{\rm rx} < 0. \tag{11}$$

The series compensation capacitor of the wireless receiver and the deployment of small balancing resistors (high ohmic value) across C_1 and C_2, ensure equal dc voltage across each capacitor under all conditions

$$V_{C1} = V_{C2} = V_{\rm dc}/2. \tag{12}$$

Using (12), (9) and (11) can be rewritten as

$$v_{\rm rx} = \text{Min}(V_{\rm dc}/2, V_{b2} - V_{\rm dc}/2) \text{ for } i_{\rm rx} > 0 \tag{13}$$

$$v_{\rm rx} = -\text{Min}(V_{\rm dc}/2, V_{b1} - V_{\rm dc}/2) \text{ for } i_{\rm rx} < 0. \tag{14}$$

During passive mode, the output voltage $V_{\rm dc}$ is defined by (13) and (14). Specifically, during each cycle of the current, $V_{\rm dc}$ can be found when

$$V_{\rm dc}/2 = V_{b2} - V_{\rm dc}/2 \text{ for } i_{\rm rx} > 0 \tag{15}$$

$$V_{\rm dc}/2 = V_{b1} - V_{\rm dc}/2 \text{ for } i_{\rm rx} < 0. \tag{16}$$

Simplifying this yields

$$V_{\rm dc} = \begin{cases} V_{b2} & \text{if } i_{\rm rx} > 0 \\ V_{b1} & \text{if } i_{\rm rx} < 0. \end{cases} \tag{17}$$

Assuming the smoothing capacitors C_1, C_2 are large such that the ripple on $V_{\rm dc}$ is small at the frequency of the receiver current, this means that the steady state voltage will be

$$V_{\rm dc} = \text{Min}(V_{b1}, V_{b2}). \tag{18}$$

Finally, the back-emf on the receiver coil can be determined by substituting (18) into (13) and (14)

$$v_{\rm rx} = \begin{cases} \text{Min}(\text{Min}(V_{b1}, V_{b2})/2, V_{b2} - \text{Min}(V_{b1}, V_{b2})/2) & \text{if } i_{\rm rx} > 0 \\ -\text{Min}(\text{Min}(V_{b1}, V_{b2})/2, V_{b1} - \text{Min}(V_{b1}, V_{b2})/2) & \text{if } i_{\rm rx} < 0. \end{cases} \tag{19}$$

While (19) is generalized solution, it can be helpful to look at the case where the batteries are equal in voltage ($V_{b1} = V_{b2} = V_b$). This significantly simplifies (19) to be simply

$$v_{\rm rx} = \begin{cases} V_b/2 & \text{if } i_{\rm rx} > 0 \\ -V_b/2 & \text{if } i_{\rm rx} < 0. \end{cases} \tag{20}$$

Another exemplary situation can be when one battery is higher than another, or $V_{b1} > V_{b2}$. In this case, (19) can be simplified as

$$v_{\rm rx} = \begin{cases} V_{b2}/2 & \text{if } i_{\rm rx} > 0 \\ -V_{b2}/2 & \text{if } i_{\rm rx} < 0. \end{cases} \tag{21}$$

A similar equation can be derived in the final case, where $V_{b1} < V_{b2}$

$$v_{\rm rx} = \begin{cases} V_{b1}/2 & \text{if } i_{\rm rx} > 0 \\ -V_{b1}/2 & \text{if } i_{\rm rx} < 0. \end{cases} \tag{22}$$

The conclusion that can be derived from the above analysis are as follows.

1) The dc-link voltage ($V_{\rm dc}$) is always equal to the voltage of the battery with the lowest voltage.
2) As a consequence, peak-to-peak back-emf voltage ($v_{\rm rx}$) is always equal to the voltage of the battery with the lowest voltage and is symmetrical (no dc component).

Finally, it can also be shown that paths associated with cases (21) and (22) can be associated with paths, which serve to charge the battery with the lowest voltage. This provides inherent ability to balance the voltage/state-of-charge of the batteries.

The power output from the receiver coil can be written as

$$P_{\rm rx} = \frac{1}{2} i_{\rm rx} v_{\rm rx} \tag{23}$$

where $v_{\rm rx}$ is defined by (19). Since the receiver coil is assumed to behave as a fixed current source, and $v_{\rm rx}$ is inherently set by

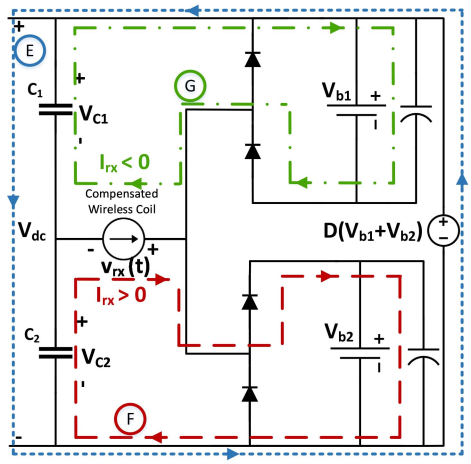

Fig. 8. Conduction paths for active mode A, where $0.5 < D < 1$ and $V_{b1} = V_{b2}$.

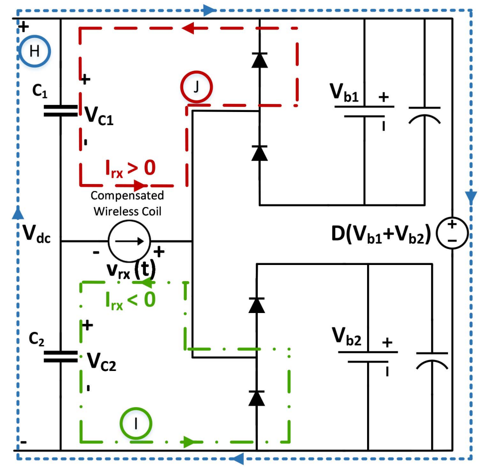

Fig. 9. Conduction paths for active mode B, where $0 < D < 0.5$ and $V_{b1} = V_{b2}$.

the battery voltages, the charging power cannot be controlled in this mode of operation.

3) Active Mode A: In order to control the charging rate of the batteries (either the overall charging power delivered, or the ratio of power delivered to each battery), the traction inverters can be activated and used as a dc/dc converter to regulate the voltage V_{dc}. The traction inverter and motor can be simplified down to a dc voltage source that sets the voltage V_{dc} as defined in (1). This means that the dc link voltage is not longer limited to always being equal to the voltage of the battery with the lowest voltage. This means that the conduction paths that are active at any given time can be intentionally controlled.

Active mode A is defined when $0.5 < D < 1$. The simplified circuit is shown in Fig. 8. During this mode of operation, the conduction path for the positive and negative half cycle can be traced by paths "F" and "G," respectively. Considering the case where $V_{b1} = V_{b2}$ for simplicity, the back-emf voltage on the receiver can be determined to be

$$v_{\mathrm{rx}} = \begin{cases} V_{b2} - V_{\mathrm{dc}}/2 & \text{if } i_{\mathrm{rx}} > 0 \\ V_{\mathrm{dc}}/2 - V_{b1} & \text{if } i_{\mathrm{rx}} < 0. \end{cases} \tag{24}$$

It is possible to change the back-emf on the receiver by changing V_{dc}, or in other words, by controlling the duty cycle D. Notice that under this mode of operation, the conduction path of the dc–dc stage (conduction loop "E") serves to charge the capacitor voltages with a dc current.

Thus, the back-emf can be written as a function of the duty as

$$v_{\mathrm{rx}} = \begin{cases} V_{b2} - \frac{D(V_{b1}+V_{b2})}{2} & \text{if } i_{\mathrm{rx}} > 0 \\ \frac{D(V_{b1}+V_{b2})}{2} - V_{b1} & \text{if } i_{\mathrm{rx}} < 0 \end{cases} \tag{25}$$

where

$$0.5 < D < 1. \tag{26}$$

In this mode of operation, the batteries are charged directly with high frequency receiver current, as visible by the conduction loops "F" and "G" in Fig. 8. Naturally, the dc-link capacitors of each inverter significantly filter any ripple current into the batteries.

4) Active Mode B: This operating mode is similar to the previous active mode, however it is defined for $0 < D < 0.5$. The main distinction from active mode A, is that the conduction paths are different. For the case where $V_{b1} = V_{b2}$, the simplified model is derived as before and shown in Fig. 9. In this case, the high frequency coil current directly charges the capacitors C_1, C_2. This can be seen from the conduction paths "J" and "I."

The back-emf is simply derived to be

$$v_{\mathrm{rx}} = \begin{cases} V_{\mathrm{dc}}/2 & \text{if } i_{\mathrm{rx}} > 0 \\ -V_{\mathrm{dc}}/2 & \text{if } i_{\mathrm{rx}} < 0. \end{cases} \tag{27}$$

Similar to before, as the receiver voltage is a function of the capacitor voltages, meaning the back-emf can be controlled by the duty cycle of the dc–dc stage. Rewriting (27) as a function of the duty cycle

$$v_{\mathrm{rx}} = \begin{cases} \frac{D(V_{b1}+V_{b2})}{2} & \text{if } i_{\mathrm{rx}} > 0 \\ -\frac{D(V_{b1}+V_{b2})}{2} & \text{if } i_{\mathrm{rx}} < 0 \end{cases} \tag{28}$$

where

$$0 < D < 0.5. \tag{29}$$

Remarkably, the back-emf is symmetrical during both cycles of the wireless ac current. This is advantageous as it means that any mismatch in battery voltages will not introduce a dc offset in the back-emf seen by the wireless receiver coil. Such a dc offset would place additional voltage stress across the compensation capacitor of the wireless receiver coil and is undesirable.

The charging power can again be controlled by adjusting the duty cycle of the dc–dc stage. In this work, this mode of operation will be used to control the charging rate of the batteries. This mode of operation limits V_{dc} to be at most equal to the average voltage of the two batteries V_{b1}, V_{b2}. This in turn, means the voltage applied to the capacitors V_{C1}, V_{C2} will be smaller then active mode A, thereby reducing the size of the capacitors required.

In active mode B, the equation for output power from the receiver coil is still the same as shown in (23). However, the key

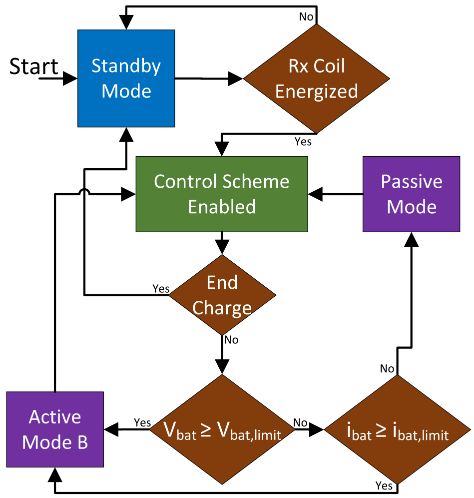

Fig. 10. Flowchart describing how to practically select between operating modes during charging.

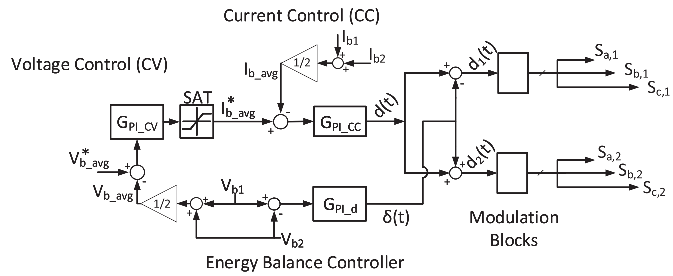

Fig. 11. Control scheme of the integrated charger.

difference is that now the receiver voltage (v_{rx} can be controlled). Using the Fourier transform, the fundamental component of the back-emf voltage can be determined to be

$$v_{\mathrm{rx}}|_{\mathrm{fund}} = \frac{4}{\pi}\frac{D(V_{b1}+V_{b2})}{2}. \tag{30}$$

Substituting the equation for the receiver back-emf in active mode B into (23), the formula for power output can be shown as a function of the duty cycle of the traction inverter

$$P_{\mathrm{rx}} = \frac{2}{\pi} i_{\mathrm{rx}} \frac{D(V_{b1}+V_{b2})}{2}. \tag{31}$$

Assuming $i_{\mathrm{rx}}, v_{\mathrm{rx}}$ are peak values, and unity power factor is guaranteed via the rectification action of the diodes.

Since the receiver current is set by the transmitter side (and held fixed), this equation shows that the power output of the receiver coil is linearly related to the duty cycle of the traction inverters (D). A duty cycle of 0.5 implies maximum power into the batteries, while also according to (4), has the least ripple current on the inductors. This is important to know, as the wireless transfer system can be optimized such that the dc/dc stage can operate at or near a duty cycle $D = 0.5$ during the majority of the charging period. This reduces losses in the machine, as well as the switches. In fact, operating at $D = 0.5$ results in the same charging power as the passive mode of operation, meaning switching can be disabled on the dc–dc stage, further reducing losses.

A flowchart regarding the operating mode logic is shown in Fig. 10. Initially, when a charging process is started, the system should begin in standby mode, which as previously described, will short-circuit the receiver coil. During this time, the receiver coil can be energized to its rated, fixed current value via the transmitter. Once the coil is energized, the control scheme is enabled to regulate the battery charging in either constant current (CC) or constant voltage (CV). At this point, if charging is finished or terminated by the user, the system can transition back to standby mode. If charging is not finished, then a choice is made to operate in either active mode or passive mode. In this case, if the battery voltage and battery current is both under the required limit, passive mode is activated. Otherwise, if the battery current/voltage is greater than or equal to the limits allowed, active mode B is engaged to maintain the charging current and voltage at the limit.

III. Control Scheme

Charging control is performed on-board the vehicle. As the vehicle drivetrain has been repurposed to serve as the power electronics of the wireless receiver, its associated digital signal processor and sensors are used to perform this control. This will make the control more robust compared to traditional control schemes, as it does not require transmitting sensitive controller feedback signals wirelessly to the transmitter. This also helps make the charging process more ubiquitous, as it reduces proprietary communications protocols.

The transmitter power electronics off-board the vehicle are not required to regulate the charging power of the batteries, and can operate at a fixed dc-bus voltage and duty cycle. They only require sensors for protective purposes (e.g., transmitter coil over-current, etc.). The charging of the batteries is fully controlled by the proposed integrated charger, and uses the control scheme shown in Fig. 11.

The controller uses three control loops, in this case implemented using proportional–integral (PI) compensators, in order to achieve CC, CV, and energy balancing between the batteries. $G_{\mathrm{PI\_CC}}$ is the PI controller, which sets the charging current into the batteries. As there are two batteries in the system, this PI controllers controls the average current into the batteries, I_{b_avg}, where

$$I_{b\_\mathrm{avg}} = \frac{I_{b1}+I_{b2}}{2}. \tag{32}$$

The reference charging current, $I^*_{b\_\mathrm{avg}}$, is set by the CV compensator, $G_{\mathrm{PI\_CV}}$. During CC operation, $I^*_{b\_\mathrm{avg}}$ is saturated to the value allowable by the battery management system (BMS), or the maximum charging power allowed from the transmitter (TX)

$$I^*_{b\_\mathrm{avg,Max}} = \mathrm{Min}(I_{b\_\mathrm{avg}}(\mathrm{BMS}), I_{b\_\mathrm{avg}}(\mathrm{TX})). \tag{33}$$

Limiting the charging current is required in order to prevent damage to the batteries and to not exceed the power rating of the wireless power transmission system.

The system enters CV operation mode when $I^*_{b\_\mathrm{avg}} < I^*_{b\_\mathrm{avg,Max}}$. Here, the CV compensator sets the average battery voltage based on the reference voltage, $V^*_{b\_\mathrm{avg}}$, set by the BMS.

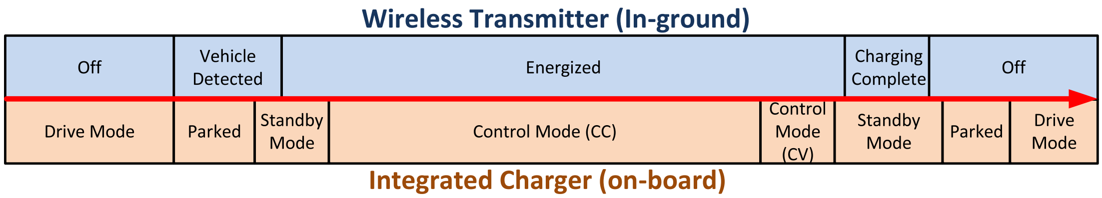

Fig. 12. Complete vehicle charging process flow, considering the in-ground transmitter and the on-board integrated charger.

The average battery voltage is defined as

$$V_{b\_\text{avg}} = \frac{V_{b1} + V_{b2}}{2}. \quad (34)$$

Finally, the last controller, G_{PI_d}, is used to balance the energy of the batteries individually. This is required as the CC/CV controllers only control the average values of the current and voltage into the batteries. Therefore, G_{PI_d} is a very slow controller, which ensures that

$$V_{b1} = V_{b2} = V_{b\_\text{avg}}. \quad (35)$$

In a system employing two identical batteries, this controller is only required to compensate for small parasitic differences, such as manufacturing tolerances, which may otherwise cause deviations from (35). G_{PI_d} works by modifying the charging distribution of the batteries by adding a small duty cycle $\delta(t)$ to the modulation of the battery with a lower voltage and subtracting the same $\delta(t)$ from the modulation of the battery with a higher voltage battery.

An overall flowchart of the states of the wireless transmitter as well as the integrated charger is shown in Fig. 12. Notice that only the following four states are required from the transmitter side.

1) Detect vehicle.
2) Power up.
3) Detect when the charging is completed and finally.
4) Power down.

Importantly, these states also do not require any communication with the receiver side (on-board) component of the wireless system. The integrated charger has the following more states.

1) Drive mode, which is used to propel the vehicle on the road.
2) Parked, which is when the vehicle is stationary and idle.
3) Standby mode, where the receiver coil is shorted.
4) Control mode (CC), where the integrated charger maintains the battery current constant.
5) Control mode (CV), where the integrated charger keeps the battery voltage constant.

The integrated charger enables its CC/CV controller after it detects that its receiver coil has coupled to a powered transmitter (as shown in Fig. 10) and regulates the charging of the batteries using the control scheme described in Fig. 11. The very simple operational requirements imposed on the transmitter can allow for a ubiquitous deployment of wireless charging stations.

TABLE II
SIMULATION AND EXPERIMENTAL PARAMETERS

Integrated Charger Parameters	Symbol	Value
Machine dc phase resistance	R_s	45 mΩ
Machine leakage inductance	L_s	0.5 mH
Battery voltages (nominal)	V_{b1}, V_{b2}	350 V
Rectifier Capacitors	C_1, C_2	20 μF
Traction inverter switching frequency	$f_{\text{sw, inv}}$	10 kHz
Wireless Parameters	**Symbol**	**Value**
Transmitter DC link	V_{in}	650 V
Transmitter full bridge switching frequency	f_{TX}	85 kHz
Transmitter Dimensions	-	650 mm × 410 mm
Transmitter Self-inductance	L_p	515 μH
Transmitter Compensation Capacitor	C_p	6.8 nF
Transmitter-Receiver Mutual inductance	M	21.5 - 24.6 μH
Receiver Dimensions	-	330 mm × 330 mm
Receiver Self-inductance	L_s	101 μH
Receiver Compensation Capacitor	C_s	34.5 nF
Misalignment (worse case)	$\Delta x, \Delta y$	75 mm, 100 mm
Coil-to-Coil Distance	z	200 mm

IV. Simulation Results

The proposed system is simulated in order to show the principle of operation. The full-switched model of the system was simulated in PLECS with the parameters given in Table II. These parameters are extracted from the developed full-scale experimental system. The mutual inductance of the coils shown are for the well-aligned case ($\Delta x = 0, \Delta y = 0$), and for the worst case misalignment (according to SAE J2954) of $\Delta x = 75$ mm, $\Delta y = 100$ mm. In this system, the vertical distance between the coils is fixed at $z = 200$ mm. This height was chosen since a dual inverter drive would most likely be employed in a larger vehicle or van.

The simulation of the system demonstrating a complete charging cycle is shown in Fig. 13, which is difficult to clearly show experimentally. Therefore, the experimental setup will be used to show fine details of the operation, as well as system dynamics and efficiency. The simple operation of the wireless system can be observed where the wireless system is simply energized at $t = 0.05$ s and turned OFF at $t = 24.5$ s. The transmitter current is relatively low, therefore incurring low ohmic losses. As expected from (28), the integrated dual inverter charger applies a low back-emf voltage (under 200 V) onto the receiver (considering it is charging an effective battery voltage of 700 V), requiring low flux levels and thus low currents in the transmitter.

The operating modes of the integrated charger can be identified in Fig. 13. The charger starts in standby mode, with the wireless receiver coil shorted (i.e., standby mode). At $t = 0.5$ s, the controller, of Fig. 11, is enabled, and transitions the system into CC mode. At this point, the dc–dc stage operates in passive

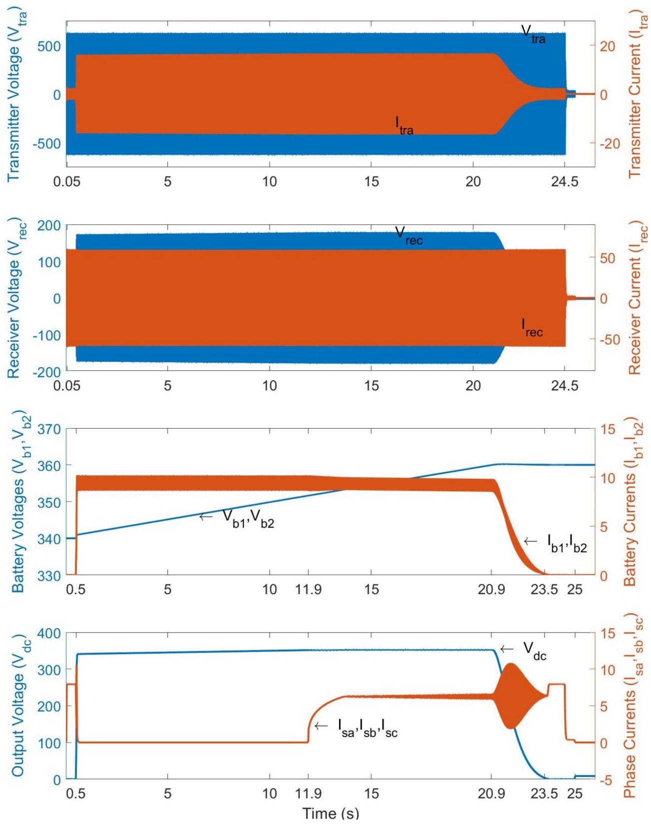

Fig. 13. Simulation of complete charging cycle, where $V^*_{b\_avg} = 360$ V and the coils are well-aligned.

mode, since the CC limit ($I_{b\_avg,Max}$) has not been reached. This mode of operation incurs no losses in the dc–dc stage, since there is no switching and no current in the traction inverters. At $t = 11.9$ s, since the battery voltages have increased, the dc–dc can no longer operate in passive mode and must start switching to regulate the charging power to be less than the CC limit (chosen such that the charging power is 6.6 kW). The effect of the dc–dc converter switching can be seen in the machine phase currents, that begin to increase with a current ripple as defined by (4). At $t = 20.9$ s, the battery reaches the CV voltage reference, $V^*_{b\_avg} = 360$ V, and the dc–dc stage transitions to CV mode of operation. In this mode, the dc–dc stage is regulating the voltage on batteries as opposed to the charging current, hence the charging current starts to decrease. The ripple in motor phases also becomes larger as the dc–dc converter duty cycle traverses from near $D = 0.5$ to $D = 0$. Note that interleaving of the dc–dc stage still ensures small ripple on the battery currents I_{b1} and I_{b2}. At $t = 23.5$ s, the CV controller has finally reached the desired voltage on the batteries and the charging is completed, therefore the dc–dc stage enters standby mode once again. Finally, once the dc–dc detects the phase current are low (signaling the wireless system has turned off), the dc-dc stage turns off at $t = 25$ s and is ready to enter drive mode.

V. Experimental Results

Experimental tests were conducted using a full-scale dual-inverter drive and 110 kW TM4 open-winding EV machine connected to a 6.6 kW wireless power transfer system (detailed in Fig. 4). The dual-inverter has two FS820R08A6P2 (820 A/750 V) traction inverter modules and the antiparallel diodes of two Wolfspeed CAS300M12BM2 (300 A/1200 V) as the additional diodes (S_1–S_4). The experimental setup parameters are similar to those in Table II, unless otherwise specified. An image of overall experimental setup is shown in Fig 14. Note that the wireless transmitter is operated at a fixed dc-link voltage ($V_{in} = 640$ V) for all of the following results.

The first test was conducted to demonstrate the operation of the charger under passive mode. This result is shown in Fig. 15. It can be seen that the wireless coils are behaving well, specifically the transmitter current (i_{tx}) is relatively low with a power factor that enables soft-switching. As shown in Fig. 6, the motor and traction inverter are disabled during passive mode, hence the machine current (i_{sa}) is zero as anticipated. In this test, the voltage of the battery 2, V_{b2}, was set to be slightly higher than the voltage of battery 1, V_{b1}, to demonstrate the inherent charge balancing described in the previous sections. As expected, the current of battery 1 is higher than the current of battery 2 ($|I_{b1}| > |I_{b2}|$). This shows that the the battery with the lowest voltage will charge with a higher current, due to the diode conduction path, as described in Section II-B. Finally, the battery currents are well filtered, due to the dc-link capacitors of the traction inverters, which are very low impedance at 85 Khz. Notice that the output voltage $V_{dc} = V_{b1} = 350$ V, which is consistent with the derivation in (18), which indicated that the output voltage will be equal to the battery with the lowest voltage.

Active mode operation is shown in Fig. 16, with $D = 0.397$. Here, the receiver is also misaligned from the transmitter, according to values given in Table II derived from the worse case misalignment allowable from the SAE J2954 standard. As expected from (1), V_{dc} is lower than in passive mode, which results in the back-emf voltage (v_{rx}) on the receiver to be reduced. The net result is that the charging power into the batteries is reduced, even though the receiver current has increased due to the misalignment. As the dc–dc stage is active and controlling V_{dc}, the motor current (i_{sa}) is nonzero. Due to the modulation strategy used for the dc–dc stage, it can be seen that the machine phase current ripple is at twice the switching frequency of the traction inverter, without any 85 kHz wireless frequency currents. There is still negligible ripple entering the batteries. Note that no shaft movement was observed in the machine, implying that no torque is generated in the machine.

The experimental measurement of the battery charging power versus duty cycle is shown in Fig. 17, demonstrating how the traction inverter can directly control the charging rate of the batteries. It can be seen that an increase in duty cycle D linearly increases the charging power, as derived in (31).

The performance of the battery current controller (G_{pi_CC}) was tested and shown in Fig. 18. This test was done by changing the average battery reference current, $I^*_{b\_avg}$, from 5 to 8 A, demonstrating the dynamic response, as well as the steady state tracking of the controller. It can be seen that the controller increases V_{dc} (by increasing the duty cycle D) in order to increase the charging current into the batteries. The change in the machine phase current can also be observed. The effect of the change in

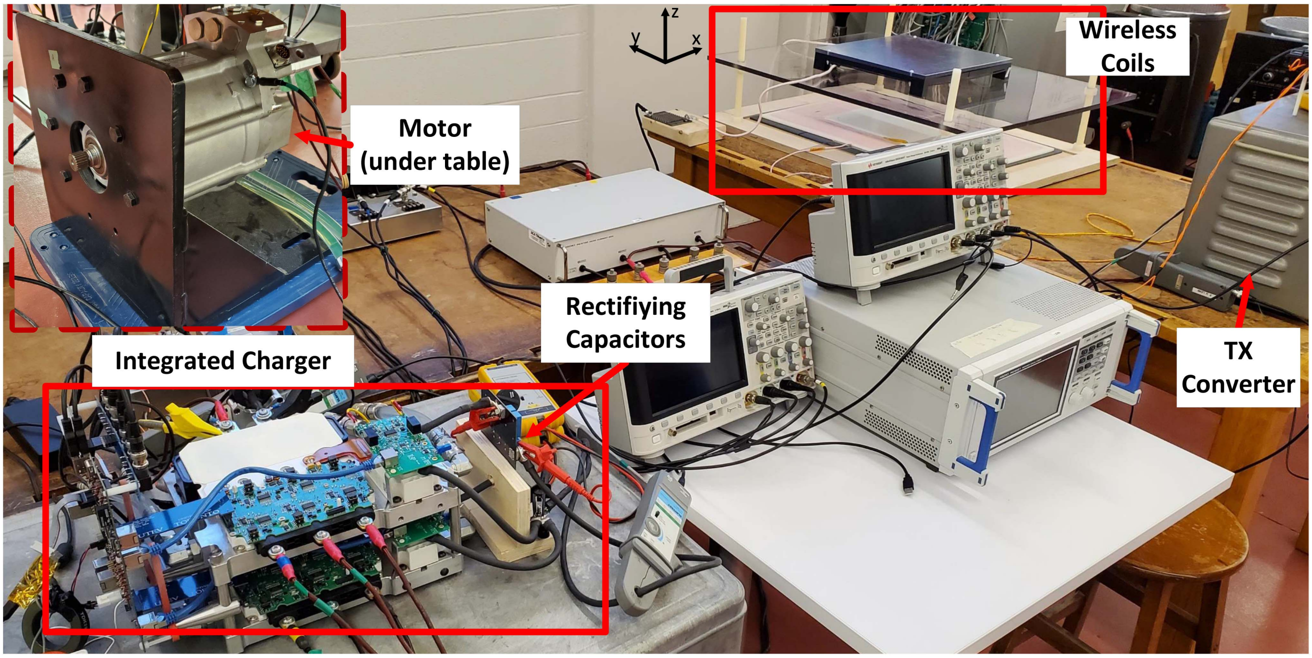

Fig. 14. Experimental setup showing the complete system.

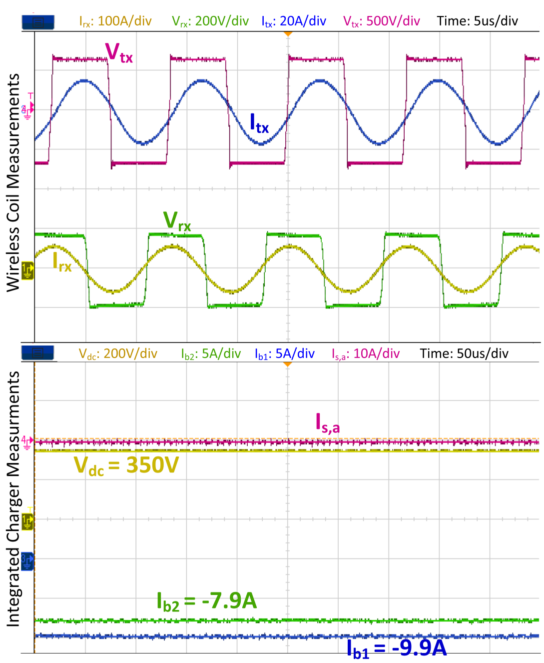

Fig. 15. System performance operating in passive mode. The inherent charge balancing is also shown, by setting $V_{b1} = 350$ V while $V_{b2} = 351$ V. Note the different timescales on the scope captures.

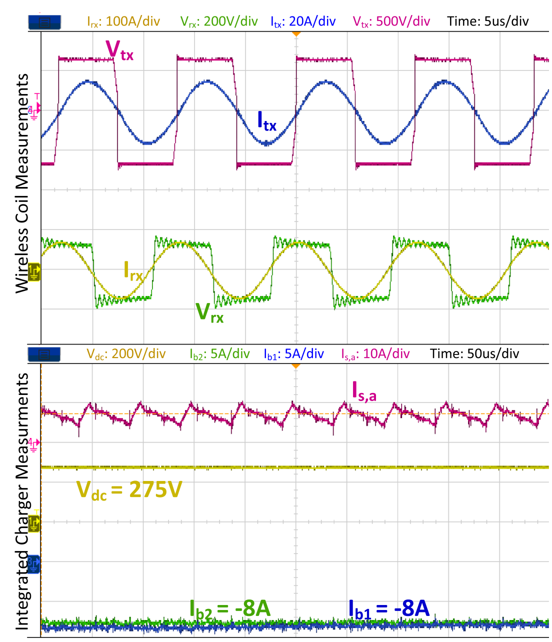

Fig. 16. System performance at maximum misalignment, in active mode with D = 0.397. Note the different timescales on the scope captures.

$V_{\rm dc}$ can be also visualized in the receiver back-emf ($v_{\rm rx}$), which is increased according to (30). Due to the chosen compensation strategy, an increase in $v_{\rm rx}$ results in an increase in the transmitter current ($i_{\rm tx}$), which can also been seen in Fig. 18.

As mentioned previously, the battery current controller only controls the average battery current. Therefore the balancing variable, $\delta(t)$, was introduced to provide individual control over the battery charging currents. The test shown in Fig. 19 was conducted while the CC controller is regulating the average battery current to be 8 A. $\delta(t)$ was changed from 0 to 0.1 instantaneously, which immediately changed the charging distribution of the batteries to be $I_{b1} = 6$ A, $I_{b2} = 10$ A. Notice that even though a step change was done on $\delta(t)$, it had no effect on the average battery controller ($G_{\rm pi\_CC}$) (or the wireless transmission system), and that the average battery current is still well regulated to 8 A.

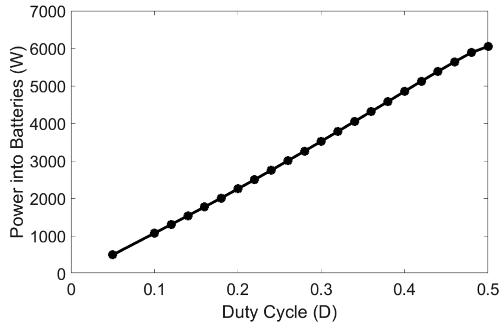

Fig. 17. Experimental measurement of battery charging power versus duty cycle of the traction inverters.

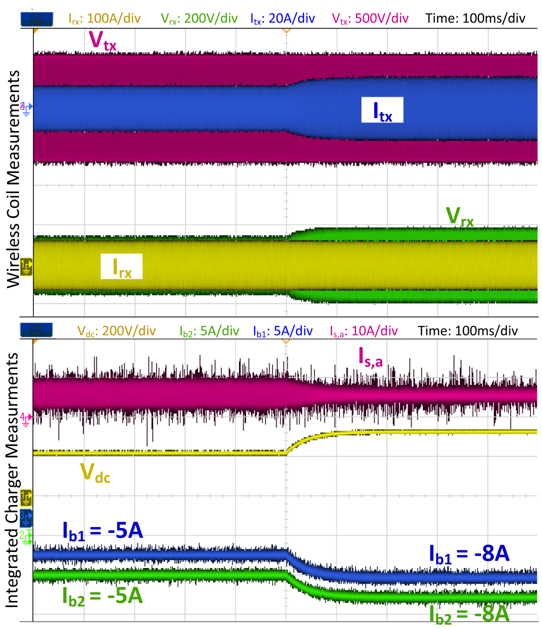

Fig. 18. Battery current step from 5 to 8 A. Note the battery currents are offset to show both clearly, however they are equal in magnitude.

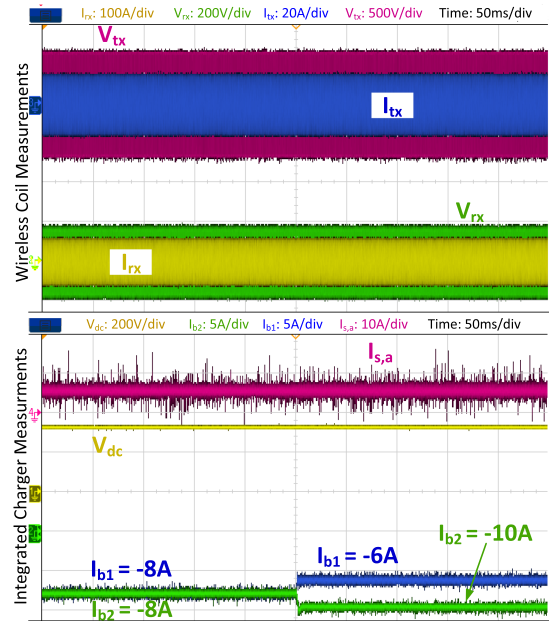

Fig. 19. A step change in $\delta(t)$ from 0 to 0.1, showing the ability of the converter to set individual battery currents, at any speed, with no controller interaction with the CC/CV average controllers.

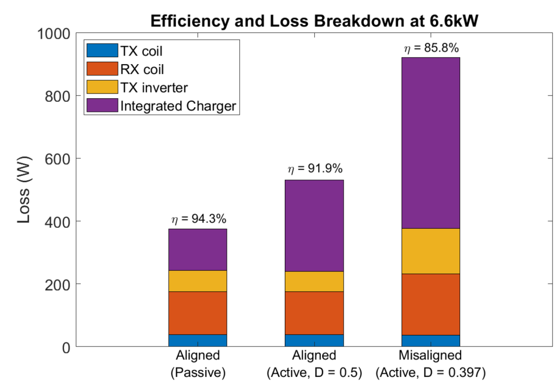

Fig. 20. Overall system efficiency, as well as loss breakdown of three main operating modes. Misaligned case assumes maximum misalignment.

Finally, the overall system efficiency was measured using a Hioki PW6001 power analyzer in order to demonstrate real-world applicability. The overall system efficiency (from the dc input of the transmitter to the batteries) is shown in Fig. 20, along with the loss breakdown in the system. As expected, the highest efficiency is achieved when the receiver-transmitter coils are aligned, and the dc–dc stage is operating in passive mode. The benefit of having low currents in the transmitter can be clearly seen here, as it exhibits very low losses. In this case, the losses in the integrated charger are simply due to the diodes (S_1–S_4) and any parasitic ohmic losses. When the dc–dc stage is operated in active mode, the losses are increased in the integrated charger, as the large 820 A IGBT modules begin switching at 10Khz, and the motor begins conducting current. However, this mode allows for the control of the charging current in the batteries. Finally, the worse case operating mode is when the receiver and transmitter coils are misaligned to the worse case values described in the SAE J2954 standard. In this case, the losses in the dc–dc stage increase, as the conducted current and ripple in the machine will increase. The current in the receiver coil also increases, since the reduced mutual coupling causes an increased current in the receiver coil. The overall system efficiency is still well above then the minimum 80% requirement of the J2954 standard. This loss breakdown is useful as it provides insight into how efficiency can be better optimized in the system, if desired. In this particular case, the dominant loss (during worse-case misalignment) is due to the traction inverters. This is expected since the 300 kW IGBT based traction inverters are being used to perform charging at 6.6 kW. The efficiency can be improved by increasing the charging power and/or using SiC-based devices which would significantly reduce the switching losses and therefore the efficiency. A comparison of efficiency to other published works is given in Table III. Compared with other integrated solutions, the efficiency of this work is higher. The work in [34] achieves higher efficiency during misalignment, however it is

TABLE III
COMPARISON OF EFFICIENCY WITH OTHER PROPOSED INTEGRATED SOLUTIONS

Ref.	Integrated system	Test power	η (aligned)	η (misaligned)
This work	Yes	6.6 kW	94.3%	85.8%
[30]	Yes	212.9 W	85.92%	-
[28]	Yes	6.6 W	88.2%	-
[35]	No	2.4 kW	91.6%	-
[34]	No	5 kW	94.5%	93.3%

a nonintegrated solution leveraging a discrete Gallium Nitride LLC converter to perform the charging control on-board the vehicle (which is a significant size/cost addition to the vehicle). Overall, these results have shown that good efficiency can still be obtained by using an integrated charging solution, which is not necessarily designed or optimized for wireless charging.

VI. CONCLUSION

This work proposed the integration of the wireless charging power electronics with the drivetrain components. Specifically, a dual-inverter drive can be used with minimal additional components to both rectify the wireless charging currents, and control the charging of the battery. These additional components can also serve as part of an integrated single-phase ac charging system. This integrated charger enables simultaneous charging of both isolated batteries in a dual-inverter drive, without requiring transmitter side control/communication. Furthermore, the high power rating of the drivetrain enables even higher power charging for no added cost. Simulation and experimental results demonstrated that full CC/CV charge control can be accomplished at 6.6 kW, using a real EV drivetrain and motor. A peak total charging efficiency of 94.3% over an airgap of 200 mm verifies real world applicability.

REFERENCES

[1] M. Y. Metwly, M. S. Abdel-Majeed, A. S. Abdel-Khalik, R. A. Hamdy, M. S. Hamad, and S. Ahmed, “A review of integrated on-board EV battery chargers: Advanced topologies, recent developments and optimal selection of FSCW slot/pole combination,” *IEEE Access*, vol. 8, pp. 85216–85242, 2020.

[2] V. Katic, I. Subotic, N. Bodo, E. Levi, B. Dumnic, and D. Milicevic, “Overview of fast on-board integrated battery chargers for electric vehicles based on multiphase machines and power electronics,” *IET Electric Power Appl.*, vol. 10, no. 3, pp. 217–229, 2016.

[3] I. Subotic and E. Levi, “A review of single-phase on-board integrated battery charging topologies for electric vehicles,” in *Proc. IEEE Workshop Elect. Machines Des., Control Diagnosis*, 2015, pp. 136–145.

[4] M. Yilmaz and P. T. Krein, “Review of battery charger topologies, charging power levels, and infrastructure for plug-in electric and hybrid vehicles,” *IEEE Trans. Power Electron.*, vol. 28, no. 5, pp. 2151–2169, May 2013.

[5] A. Khaligh and S. Dusmez, “Comprehensive topological analysis of conductive and inductive charging solutions for plug-in electric vehicles,” *IEEE Trans. Veh. Technol.*, vol. 61, no. 8, pp. 3475–3489, Oct. 2012.

[6] M. Y. Metwly et al., “Investigation of six-phase surface permanent magnet machine with typical slot/pole combinations for integrated onboard chargers through methodical design optimization,” *IEEE Trans. Transport. Electrific.*, vol. 9, no. 1, pp. 866–885, Mar. 2023.

[7] A. Cordeiro, V. F. Pires, D. Foito, and J. F. Silva, “A three-phase on-board integrated battery charger for EVS using a drive based on triple inverters,” in *IECON 48th Annu. Conf. IEEE Indust. Electron. Soc.*, 2022, pp. 1–6.

[8] G. Pellegrino, E. Armando, and P. Guglielmi, “An integral battery charger with power factor correction for electric scooter,” *IEEE Trans. Power Electron.*, vol. 25, no. 3, pp. 751–759, Mar. 2010.

[9] B. Brian and S. Loudot, “Rapid reversible charging device for an electric vehicle,” U.S. Patent 20110254494A1, Oct., 2011.

[10] S. Loudot, B. Briane, O. Ploix, and A. Villeneuve, “Rapid reversible charging device for an electric vehicle,” U.S. Patent 8847555B2, Sep., 2014.

[11] S. Semsar, T. Soong, and P. W. Lehn, “On-board single-phase integrated electric vehicle charger with V2G functionality,” *IEEE Trans. Power Electron.*, vol. 35, no. 11, pp. 12072–12084, Nov. 2020.

[12] A. Ahmad, M. S. Alam, and R. Chabaan, “A comprehensive review of wireless charging technologies for electric vehicles,” *IEEE Trans. Transp. Electrific.*, vol. 4, no. 1, pp. 38–63, Mar. 2018.

[13] C. R. Teeneti, T. T. Truscott, D. N. Beal, and Z. Pantic, “Review of wireless charging systems for autonomous underwater vehicles,” *IEEE J. Ocean. Eng.*, vol. 46, no. 1, pp. 68–87, Jan. 2021.

[14] Z. Zhang and B. Zhang, “Angular-misalignment insensitive omnidirectional wireless power transfer,” *IEEE Trans. Indust. Electron.*, vol. 67, no. 4, pp. 2755–2764, Apr. 2020.

[15] Y. Li, J. Zhao, Q. Yang, L. Liu, J. Ma, and X. Zhang, “A novel coil with high misalignment tolerance for wireless power transfer,” *IEEE Trans. Magn.*, vol. 55, no. 6, Jun. 2019, Art. no. 2800904.

[16] Y. Liu, U. K. Madawala, R. Mai, and Z. He, “Zero-phase-angle controlled bidirectional wireless ev charging systems for large coil misalignments,” *IEEE Trans. Power Electron.*, vol. 35, no. 5, pp. 5343–5353, May 2020.

[17] M. Pathmanathan, S. Nie, N. Yakop, and P. W. Lehn, “Field-oriented control of a three-phase wireless power transfer system transmitter,” *IEEE Trans. Transp. Electrific.*, vol. 5, no. 4, pp. 1015–1026, Dec. 2019.

[18] Z. Luo, Y. Zhao, M. Xiong, X. Wei, and H. Dai, “A self-tuning LCC/LCC system based on switch-controlled capacitors for constant-power wireless electric vehicle charging,” *IEEE Trans. Indust. Electron.*, vol. 70, no. 1, pp. 709–720, Jan. 2023.

[19] N. Fu, J. Deng, Z. Wang, and D. Chen, “An LCC–LCC compensated wpt system with switch-controlled capacitor for improving efficiency at wide output voltages,” *IEEE Trans. Power Electron.*, vol. 38, no. 7, pp. 9183–9194, Jul. 2023.

[20] B. Sanftl, F. Pflaum, M. Trautmann, R. Weigel, and A. Koelpin, “A novel approach for reliable communications within inductive power transfer systems,” in *Proc. IEEE Wireless Power Transfer Conf.*, 2016, pp. 1–4.

[21] Z. Li, K. Song, C. Zhu, R. Lu, and G. Wei, “Constant current charging for variable load employing secondary side controlled wireless charging system,” in *Proc. IEEE Transp. Electrific. Conf. Expo., Asia-Pacific (ITEC Asia-Pacific)*, 2017, pp. 1–6.

[22] K. Song et al., “Constant current charging and maximum system efficiency tracking for wireless charging systems employing dual-side control,” *IEEE Trans. Indust. Appl.*, vol. 56, no. 1, pp. 622–634, Jan./Feb. 2020.

[23] Z. Li, K. Song, J. Jiang, and C. Zhu, “Constant current charging and maximum efficiency tracking control scheme for supercapacitor wireless charging,” *IEEE Trans. Power Electron.*, vol. 33, no. 10, pp. 9088–9100, Oct. 2018.

[24] V. P. Galigekere, O. C. Onar, M. Chinthavali, and Z. J. Wang, “Load power agnostic 6.6 kw wireless EV charger with LCL tuned primary and secondary side regulation,” in *Proc. IEEE Energy Convers. Congr. Expo.*, 2017, pp. 4839–4844.

[25] T. Hiramatsu, X. Huang, M. Kato, T. Imura, and Y. Hori, “Wireless charging power control for HESS through receiver side voltage control,” in *Proc. IEEE Appl. Power Electron. Conf. Expo.*, 2015, pp. 1614–1619.

[26] K. Matsuura, D. Kobuchi, Y. Narusue, and H. Morikawa, “Communication-less receiver-side resonant frequency tuning for magnetically coupled wireless power transfer systems,” *IEEE Access*, vol. 11, pp. 23544–23556, 2023.

[27] A. Ramezani and M. Narimani, “Optimal design of fully integrated magnetic structure for wireless charging of electric vehicles,” *IEEE Trans. Transport. Electrific.*, vol. 7, no. 4, pp. 2114–2127, Dec. 2021.

[28] M. Chinthavali, O. C. Onar, S. L. Campbell, and L. M. Tolbert, “Integrated charger with wireless charging and boost functions for PHEV and EV applications,” in *Proc. IEEE Transp. Electrific. Conf. Expo. (ITEC)*, 2015, pp. 1–8.

[29] J. Mahlein, J. Kollar, M. Lawandowski, M. Hauck, L. Podbielski, and J. Schmidt, “Drive system, method for operating a drive system, and use,” U.S. Patent 8912738B2, Dec. 2014.

[30] S. R. Meher and R. K. Singh, "A multimode power processor with wired and wireless battery charging for electric vehicle," *IEEE Trans. Indust. Electron.*, early access, May 22, 2023, doi: 10.1109/TIE.2023.3277094.

[31] M. Pathmanathan, S. Nie, N. Yakop, and P. Lehn, "Efficiency improvement of a wireless power transfer system using a receiver side voltage doubling rectifier," in *Proc. 21st Eur. Conf. Power Electron. Appl. (EPE'19 ECCE Eur.)*, 2019, pp. P.1–P.8.

[32] W. Zhang and C. C. Mi, "Compensation topologies of high-power wireless power transfer systems," *IEEE Trans. Veh. Technol.*, vol. 65, no. 6, pp. 4768–4778, Jun. 2016.

[33] R. Shi, S. Semsar, and P. W. Lehn, "Constant current fast charging of electric vehicles via a dc grid using a dual-inverter drive," *IEEE Trans. Indust. Electron.*, vol. 64, no. 9, pp. 6940–6949, Sep. 2017.

[34] M. Elshaer, C. Bell, A. Hamid, and J. Wang, "Dc–dc topology for interfacing a wireless power transfer system to an on-board conductive charger for plug-in electric vehicles," *IEEE Trans. Indust. Appl.*, vol. 57, no. 6, pp. 5552-5561, Nov./Dec. 2021.

[35] Q. Deng et al., "Wired/wireless hybrid charging system for electrical vehicles with minimum rated power requirement for DC module," *IEEE Trans. Veh. Technol.*, vol. 69, no. 10, pp. 10889–10898, Oct. 2020.

Sepehr Semsar (Member, IEEE) received the B.A.Sc. and Ph.D. degrees in electrical engineering from the University of Toronto, Toronto, ON, Canada, in 2016 and 2022, respectively.

He is currently working as a Senior Electrical Engineer with eLeapPower. His research interests include power electronics, electric vehicle drivetrains, charging systems, and high efficiency dc–dc/dc–ac converters.

Zhichao Luo (Member, IEEE) received the B.S. degree in automotive engineering from the South China University of Technology, Guangzhou, China, in 2014 and the Ph.D. degree in automotive engineering from Tongji University, Shanghai, China, in 2019.

From 2019 to 2021, he was a Postdoctoral Fellow with the Department of Electrical and Computer Engineering, University of Toronto, Toronto, ON, Canada. From 2021 to 2023, he worked as a Postdoctoral Research Associate with the University of Cambridge, Cambridge, U.K. In 2023, he joined the School of Electric Power Engineering with the South China University of Technology, where he is currently an Associate Professor. His current research interests include wireless power transfer technologies, high-frequency magnetic components, novel soft magnetic material, magnetic field modeling, and power electronics in electric vehicles.

Dr Luo was the Industry Liaison chair of TC9: Wireless Power Transfer Systems in PELS.

Shuang Nie (Member, IEEE) received the B.A.Sc. (Hons.) and M.A.Sc. degrees in electrical and computer engineering in 2017 and 2019, respectively, from the University of Toronto, Toronto, ON, Canada, where he is currently working toward the Ph.D. degree in electrical and computer engineering.

His research interests include the energy system modeling, optimization, wireless power transfer technologies, and wireless charging for electric vehicles.

Peter W. Lehn (Senior Member, IEEE) received the B.Sc. and M.Sc. degrees in electrical engineering from the University of Manitoba, Winnipeg, MN, Canada, in 1990 and 1992, respectively, and the Ph.D. degree in electrical engineering from the University of Toronto, Toronto, Canada, in 1999.

He joined the faculty with the University of Toronto, in 1999. He spent six months as Visiting Professor with the University of Erlangen-Nuremberg, Erlangen, Germany, in 2001. His research interests include HVDC technologies, grid integration of storage and renewables, power electronics for electric vehicles, and theoretical analysis of power electronic systems.

Dr. Lehn has been an Editor of IEEE TRANSACTIONS ON ENERGY CONVERSION from 2013 to 2019.